A FOM suitable for characterizing a frequency divider is defined as follows [7]:

$$\mathrm{FOM}[\mathrm{GHz}^2/\mathrm{mW}] = \frac{f_{\mathrm{H}}[\mathrm{GHz}] \cdot f_{\mathrm{lock}}[\mathrm{GHz}]}{\mathrm{PD}[\mathrm{mW}]} \quad (3)$$

where f_{H}[GHz] represents the highest operating frequency in GHz, f_{lock}[GHz] represents the locking frequency range in GHz, and PD presents the power consumption in mW. Table 1 is a summary of the implemented ILFD3, and recently reported state-of-the-art divide-by-3 CMOS dividers in Refs. 2, 4–6. As can be seen, our ILFD3 showed the widest LR, and achieved the highest FOM. The results indicate that the ILFD3 topology is very suitable for Ka-band and even higher frequency band communication system applications.

4. CONCLUSIONS

In this work, we report a 31.29–38.18 GHz CMOS ILFD3 with 19.84% LR. Divide-by-3 and low-voltage operations were achieved by the differential-injection linear mixers, which constitute two source-connected series NMOSFETs in parallel with the LC tank and cross-coupled transistors. The merit of wide LR is mainly attributed to the adoption of two pairs of varactors to enhance the ratio of variable capacitance to the overall capacitance of the LC tank. On the other hand, low output phase-noise is partly attributed to the addition of a bypass capacitor to the drain terminal of the head current source to eliminate its noise contribution. The results indicate that the proposed ILFD3 topology is suitable for Ka-band communication system applications.

ACKNOWLEDGMENTS

This work was supported by the National Science Council of the R.O.C. under Contracts NSC-97-2221-E-260-009-MY3 and NSC 97-2221-E-260-010-MY3. The authors are very grateful for the support from the National Chip Implementation Center (CIC), Taiwan, for chip fabrication and measurements, and National Nano-Device Laboratory (NDL), Taiwan, for measurements.

REFERENCES

1. H. Wu and L. Zhang, A 16-to-18 GHz 0.18 μm Epi-CMOS divide-by-3 injection-locked frequency divider, In: IEEE ISSCC Tech. Dig., 2006, pp.27–29.
2. S.L. Jang, C.W. Chang, W.C. Cheng, C.F. Lee, and M.H. Juang, Low-power divide-by-3 injection- locked frequency dividers implemented with injection transformers, Electron Lett 45 (2009), 240–241.
3. S.L. Jang, C.Y. Lin, and C.F. Lee, A low voltage 0.35 μm CMOS frequency divider with the body injection technique, IEEE Microwave Wireless Compon Lett18(2008).
4. S. Rong and H.C. Luong, A 1.7 mW 25 GHz transformer-feedback divide-by-3 frequency divider with quadrature outputs, IEEE Asian Solid-State Circuits Conference 2007, Korea,2007, pp.328–331.
5. S.L. Jang, W. Yeh, and C.F. Lee, A low power CMOS divide-by-3 LC-tank injection locked frequency divider, Microwave Opt Technol Lett 50 (2008), 259–263.
6. C.F. Lee and S.L. Jang, A novel divide-by-3 hartley injection-locked frequency divider, Microwave Opt Technol Lett 50 (2008), 906–909.
7. T.N. Lu and Y.J.E. Chen, A 0.8-mW 55-GHz dual-injection-locked CMOS frequency divider, IEEE Trans Microwave Theory Tech56(2008).

BOUNDARY CONDITION FOR THE EFFICIENT EXCITATION AND ABSORPTION OF HYBRID WAVEGUIDE MODES IN FINITE ELEMENT FORMULATIONS

Odysseas Tsilipakos, Emmanouil E. Kriezis, and Traianos V. Yioultsis
Department of Electrical and Computer Engineering, Aristotle University of Thessaloniki, Thessaloniki GR-54124, Greece; Corresponding author: otsilipa@auth.gr

Received 14 February 2011

ABSTRACT: *A boundary condition capable of efficiently exciting and absorbing hybrid waveguide modes is derived for use in the context of the finite element method. Its performance is assessed in two cases, that is, a silicon and a plasmonic waveguide, and compared with that of the standard absorbing boundary condition.* © 2011 Wiley Periodicals, Inc. Microwave Opt Technol Lett 53:2626–2631, 2011; View this article online at wileyonlinelibrary.com. DOI 10.1002/mop.26364

Key words: *finite element method; guided-wave devices; absorbing boundary condition; hybrid waveguide modes; optical waveguides*

1. INTRODUCTION

The finite element method (FEM) [1] is one of the most prominent numerical techniques for the analysis of complex high-frequency electromagnetic problems. These include radiation, scattering, and guided-wave problems spanning frequencies from the microwave to the optical regime. Among its advantages is the use of unstructured meshes and isoparametric elements, conforming with the boundaries of curved geometrical objects. Moreover, by using proper (curl-conforming) vector basis functions, the tangential field continuity at interfaces between different materials is inherently satisfied. Therefore, there is neither a need for explicitly enforcing it nor for adopting averaging schemes to mitigate abrupt discontinuities in material parameters, as customarily done in finite difference–based methods. Finally, the resulting matrices are sparse (e.g., contrary to integral equation methods), and thus the linear system of equations can be efficiently solved even for very high numbers of unknowns (degrees of freedom [DoFs]).

To date, the FEM has experienced widespread use in modeling guided-wave devices or waveguide discontinuities [2–4]. A crucial issue in such problems is the efficient implementation of the input-port boundary condition, assigned with the task of exciting and at the same time absorbing the guided mode. The reflectionless truncation of the output waveguide(s) is also important, but for this case, except for the absorbing boundary condition (ABC) option, there is always the alternative of using perfectly matched layers (PMLs). Furthermore, if the waveguide is open, the remaining sides of the bounding box, that is, the side-walls, can be appointed first- or higher-order plane-wave ABCs. Alternatively, they can be coated with PMLs. It is the input-port that cannot be implemented any other way but with an ABC and hence its performance is crucial.

So far, in most of the analyzed structures the underlying waveguide supports a quasi-TEM or purely TE/TM mode. For example, this is the case with microstrips (fundamental mode) and rectangular metallic waveguides. This translates into scalar and constant (spatially invariant) wave impedances characterizing the supported modes. As a result, the implementation of the input-

port ABC is rather straightforward [1, 3]. However, most modern waveguides of optical and microwave/millimeter-wave technology support hybrid modes, meaning that all six field components are nonzero. More importantly, the mode wave impedances are spatially dependent (functions of the cross-sectional coordinates) and of tensorial nature. Examples of such waveguides are wire and rib waveguides based on the silicon-on-insulator technology, plasmonic waveguides such as the dielectric-loaded, channel, stripe, or conductor-gap-silicon (CGS) waveguide, as well as inhomogeneous millimeter-wave waveguides such as the finline [5], or the (shielded) image line.

In the present work, we develop an input-port boundary condition capable of efficiently exciting and absorbing hybrid waveguide modes. The performance of the proposed ABC is tested in two examples and compared with that of the standard ABC derived for quasi-TEM or purely TE modes.

2. BOUNDARY CONDITION DERIVATION

Consider a guided-wave device based on any kind of optical or microwave/millimeter-wave waveguide and let us focus on the input port (S_1) at which the mode is fed (Fig. 1). For the purpose of deriving an ABC capable of efficiently exciting (while simultaneously absorbing) a hybrid waveguide mode, we start from a generalized orthogonality condition relating the transverse electric and magnetic field components

$$\mathbf{H}_t = \frac{\hat{\mathbf{k}} \times \mathbf{E}}{\bar{\bar{Z}}_w}. \tag{1}$$

The wave impedance is not scalar because the mode in question is neither purely TE nor purely TM. Rather, it is a dyadic tensor given by

$$\bar{\bar{Z}}_w = Z_w^{\mathrm{TM}}(u,v)\hat{\mathbf{u}}\hat{\mathbf{u}} + Z_w^{\mathrm{TE}}(u,v)\hat{\mathbf{v}}\hat{\mathbf{v}}, \tag{2}$$

where $\hat{\mathbf{u}}$ and $\hat{\mathbf{v}}$ are two orthogonal tangential unit vectors on S_1 and the respective wave impedances are defined through

$$Z_w^{\mathrm{TE}}(u,v) = \frac{E_u(u,v)}{H_v(u,v)}, \quad Z_w^{\mathrm{TM}} = -\frac{E_v(u,v)}{H_u(u,v)}. \tag{3}$$

Returning to Eq. (1), we take the cross product with the outward-pointing normal-to-S_1 unit vector $\hat{\mathbf{n}}$

$$\hat{\mathbf{n}} \times \mathbf{H}_t \equiv \hat{\mathbf{n}} \times \mathbf{H} = \hat{\mathbf{n}} \times \frac{1}{\bar{\bar{Z}}_w}\hat{\mathbf{k}} \times \mathbf{E}, \tag{4}$$

which, by making use of Faraday's law, can be written as

$$\hat{\mathbf{n}} \times \nabla \times \mathbf{E} = -j\omega\mu_0 \hat{\mathbf{n}} \times \frac{1}{\bar{\bar{Z}}_w}\hat{\mathbf{k}} \times \mathbf{E}. \tag{5}$$

By combining two such equations, one for the incident ($\hat{\mathbf{k}} \equiv -\hat{\mathbf{n}}$ and one for the reflected ($\hat{\mathbf{k}} \equiv \hat{\mathbf{n}}$) field, and noting that $\mathbf{E} = \mathbf{E}^{\mathrm{inc}} + \mathbf{E}^{\mathrm{ref}}$ we arrive at

$$\hat{\mathbf{n}} \times \nabla \times \mathbf{E} + j\omega\mu_0 \hat{\mathbf{n}} \times \bar{\bar{Z}}_w^{-1}\hat{\mathbf{n}} \times \mathbf{E} = 2j\omega\mu_0 \hat{\mathbf{n}} \times \bar{\bar{Z}}_w^{-1}\hat{\mathbf{n}} \times \mathbf{E}^{\mathrm{inc}}, \tag{6}$$

which is none other than the ABC with concomitant excitation we were looking for. Equation (6) can be written in a more concise manner as

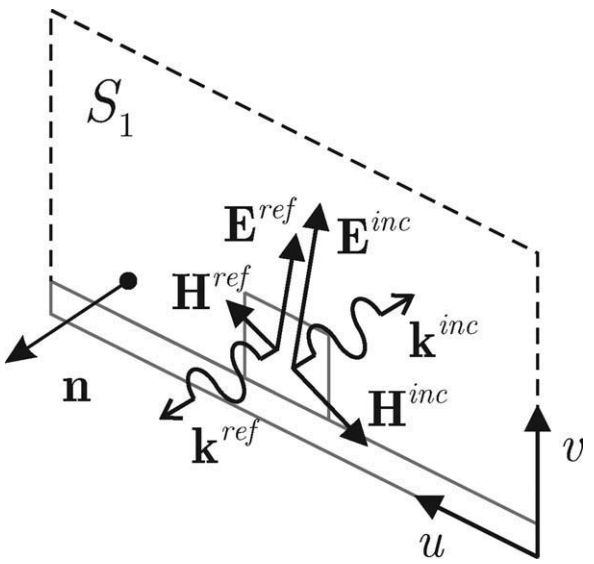

Figure 1 Input-port of a waveguide-based circuit with incident and reflected fields

$$\hat{\mathbf{n}} \times \nabla \times \mathbf{E} + \bar{\bar{\gamma}}\hat{\mathbf{n}} \times \hat{\mathbf{n}} \times \mathbf{E} = 2\bar{\bar{\gamma}}\hat{\mathbf{n}} \times \hat{\mathbf{n}} \times \mathbf{E}^{\mathrm{inc}}, \tag{7}$$

where

$$\bar{\bar{\gamma}} = \frac{j\omega\mu_0}{Z_w^{\mathrm{TE}}(u,v)}\hat{\mathbf{u}}\hat{\mathbf{u}} + \frac{j\omega\mu_0}{Z_w^{\mathrm{TM}}(u,v)}\hat{\mathbf{v}}\hat{\mathbf{v}}. \tag{8}$$

Note that now the $\hat{\mathbf{u}}\hat{\mathbf{u}}$ dyad involves the TE instead of the TM wave impedance. Equation (7) permits a direct comparison with the standard input-port ABC [1, 3]

$$\hat{\mathbf{n}} \times \nabla \times \mathbf{E} + j\beta\hat{\mathbf{n}} \times \hat{\mathbf{n}} \times \mathbf{E} = 2j\beta\hat{\mathbf{n}} \times \hat{\mathbf{n}} \times \mathbf{E}^{\mathrm{inc}}, \tag{9}$$

derived for quasi-TEM, or purely TE modes, to be made. Specifically, by observing Eqs. (7) and (9), one can readily verify that Eq. (9) amounts to admitting that the wave impedance is scalar and moreover has a spatially constant value of η_0/n_{eff}. However, neither of the above is true in the case of a hybrid waveguide mode. Finally, let us just note that compared with Eq. (7), we prefer the form of Eq. (6), because it is more convenient in view of the Galerkin procedure followed for the discretization of the governing equations.

The output-port ABC, assigned with the task of only absorbing a hybrid waveguide mode, is simply given by Eq. (6) with a zero right-hand side, that is,

$$\hat{\mathbf{n}} \times \nabla \times \mathbf{E} + j\omega\mu_0 \hat{\mathbf{n}} \times \bar{\bar{Z}}_w^{-1}\hat{\mathbf{n}} \times \mathbf{E} = \mathbf{0}. \tag{10}$$

A similar boundary condition (along with a plane-wave excitation part) has been used for the truncation of scattering problems in the context of the three-dimensional (3D)-FEM/adaptive-ABC method [1, 5, 6]. Obviously, the advantage in guided wave problems is that the field distribution on the output-port is a priori known, and, thus, there is no need for following an adaptive procedure. It should be noted that as the output port ABC is designed for absorbing a single-guided mode, the output port should be placed sufficiently far from any discontinuities that

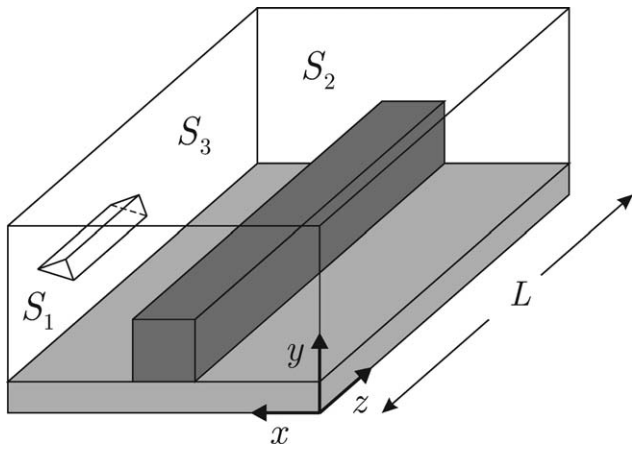

Figure 2 Straight waveguide segment truncated by fictitious input (S_1) and output (S_2) ports separated by a distance L. Side walls are denoted by S_3. The orientation of the prism-element mesh is also depicted

might excite higher-order or radiation modes. Clearly, this holds for the input port as well.

3. NUMERICAL ASSESSMENT AND DISCUSSION

In this section, we assess the performance of the proposed boundary condition and have compared it against the standard ABC. For this purpose, we consider a straight waveguide segment truncated by fictitious input and output ports separated by a distance L (Fig. 2). At the input port (S_1), Eq. (6) is used for exciting the waveguide mode (with unit amplitude of the dominant electric-field component), while Eq. (1) is used for the absorption of the mode at the output-port (S_2). In what follows, two optical waveguides are examined, namely a silicon wire and a CGS plasmonic waveguide. As both waveguides considered are open, first-order plane-wave ABCs:

$$\hat{\mathbf{n}} \times \nabla \times \mathbf{E} + jk\hat{\mathbf{n}} \times \hat{\mathbf{n}} \times \mathbf{E} = \mathbf{0}, \tag{11}$$

are implemented on the side-walls (S_3) of the computational domain. Although of minor importance in the case of a straight undisrupted waveguide, this would become necessary in the event of any waveguide discontinuities that would excite radiation modes.

Returning to Figure 2, we note that it is the x and y coordinates that are assigned to the waveguide cross-section, that is, $u \equiv x$ and $v \equiv y$ with respect to Figure 1, and, thus, the normal unit vector of the input port coincides with $-\hat{\mathbf{z}}$. Discretization of the structure is performed by first-order prism elements (curl complete to order zero) [7–9]. The prism axis is oriented along the propagation direction, that is, the z-axis (Fig. 2). Therefore, it is the triangular faces of the prisms that tessellate the waveguide cross-section. We should note, however, that the conclusions drawn in the following subsections hold for any other prism orientation or even element type, for example, tetrahedral or brick.

To implement the input- and output-port ABCs in the 3D-guided-wave problem, one must first solve a two-dimensional (2D) eigenvalue problem of the waveguide cross-section. Having solved for the supported mode, we have access to the three components of the electric field and the three components of the magnetic field through differentiation (or vice versa). It is, therefore, straightforward to implement the input- and output-port ABCs and obtain a solution for the 3D problem. Clearly, a purely guided wave is expected to propagate in the simulated structure, provided, of course, that the boundary conditions work

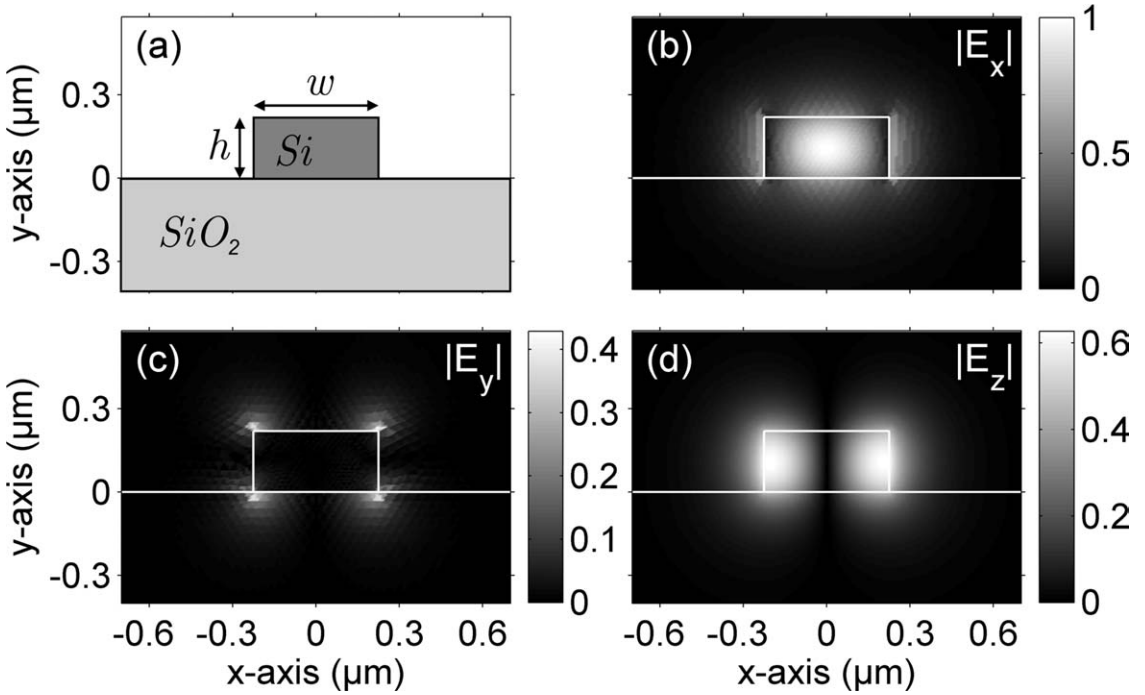

Figure 3 (a) Cross-section of the silicon-wire waveguide. (b)–(d) Electric field components (absolute value) for the fundamental TE mode at an operating wavelength of 1.55 μm

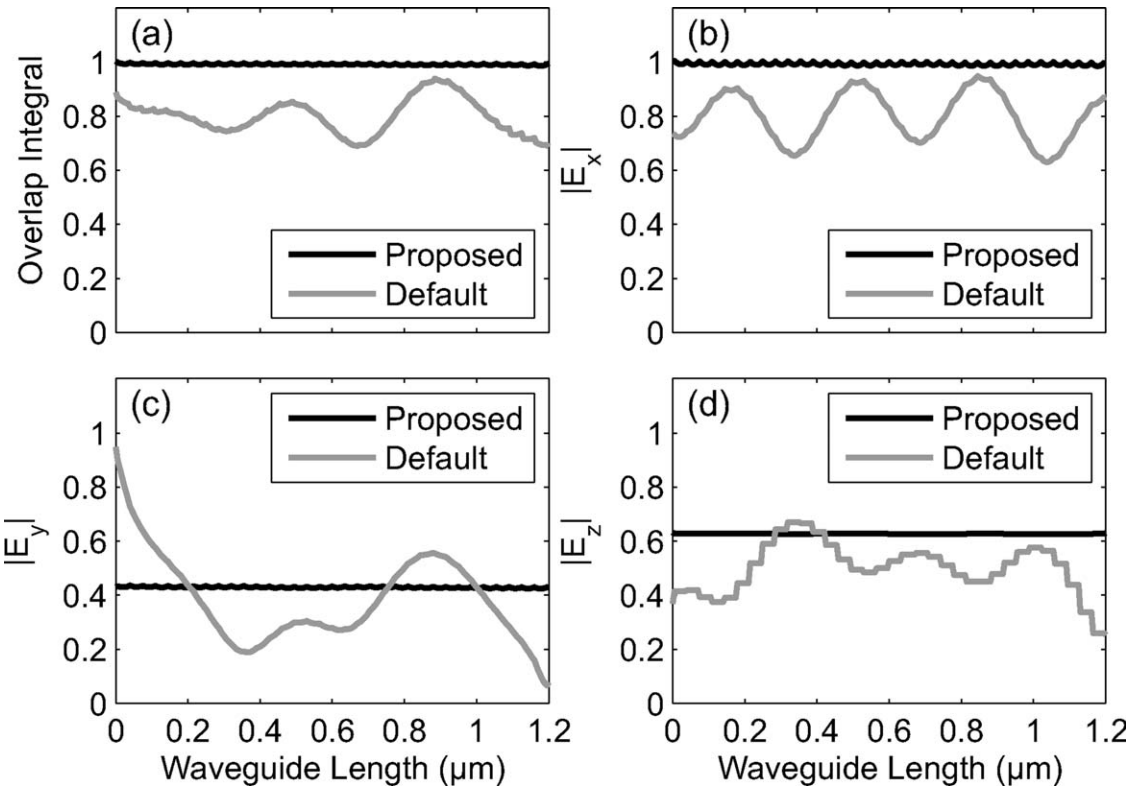

Figure 4 Comparison between proposed and default absorbing boundary conditions for a 1.2-μm-long silicon wire waveguide operating on the fundamental TE mode at the 1.55 μm telecommunication wavelength. (a) Overlap integral along the waveguide, and (b)–(d) absolute value of electric field components along the waveguide. Each component is evaluated at the cross-sectional point associated with its peak value

correctly. On the other hand, if the performance of the boundary conditions is not satisfactory, a standing-wave pattern is bound to appear, owing to reflections from the two ports.

3.1 Silicon Wire

As a first example, we consider a silicon wire, which consists of a silicon ($n_{Si} = 3.45$) ridge residing on a silica ($n_{SiO_2} = 1.45$) substrate [Fig. 3(a)]. The ridge dimensions are set to $w \times h = 450 \times 220$ nm^2, which are typical for such waveguides [10]. The fundamental mode in this case is TE-like. This means that E_∞ is the dominant electric field component. As mentioned earlier, first a 2D-eigenvalue problem of the waveguide cross section is solved to get hold of the mode field components. The absolute value of the electric field components corresponding to the fundamental TE mode for an operating wavelength of 1.55 μm are depicted in Figure 3(b)–(d). One can readily verify the hybrid nature of the mode in question by noting that the two transverse components are of comparable magnitude. Alternatively, this can be confirmed by the fact that both axial components (electric and magnetic) are nonzero.

Subsequently, we turn to the 3D-guided-wave problem. The length of the waveguide segment considered is $L = 1.2$ μm, corresponding to $\sim 1.73\lambda_g$ for the mode in question ($\lambda_g \sim 0.692$ μm at the free-space wavelength of 1.55 μm). Regarding the discretization of the 3D structure, the axial mesh density is $\sim$20 points per guide wavelength, that is, the prisms are approximately $\lambda_g/20$ long. Moreover, the cross-sectional (triangular) mesh is identical with that of the 2D eigenvalue problem. Solving the 3D problem, we obtain the E-field in the entire structure. We solve the problem twice, considering both the proposed [Eq. (6)] and default [Eq. (9)] ABCs, to provide a comparison between the two.

In Figure 4(b)–(d) we plot the absolute value of the electric field components along the waveguide for the two cases. Each component is evaluated at the cross-sectional point associated with its peak value, that is, at the center of the ridge for E_∞ and at the corner and vertical edge of the ridge for E_y and E_z, respectively (Fig. 3). As is evident from Figure 4, when the proposed boundary condition is used (black curves), all the three components acquire the correct amplitude at the input port ($z = 0$) and retain that exact value along the waveguide, indicating that a purely guided wave is propagating in the structure. On the other hand, when the standard ABC is used (gray curves), the mode is not correctly excited at the input port, that is, the value and relative amplitude of the three field components at $z = 0$ is different than what dictated by the eigenvalue problem. More importantly, there is a clear oscillatory pattern with a period of $\lambda_g/2$, indicative of a standing wave.

Plots (b)–(d) in Figure 4 examine the behavior of the electric-field components at a single cross-sectional point, that associated with each component's peak value. To obtain a measure of the boundary condition performance involving the entire waveguide cross section, we make use of a vector overlap integral correlating the actually propagating mode along the waveguide with the reference one, which is simply the solution of the eigenvalue problem. The overlap integral chosen is of the following form

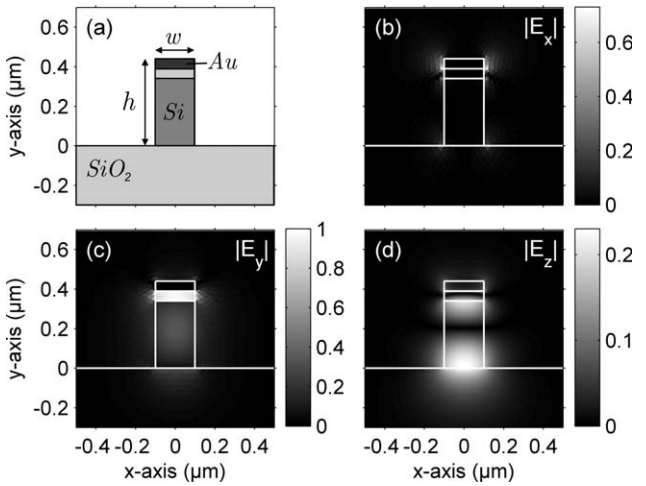

Figure 5 (a) Cross section of the CGS plasmonic waveguide. (b)–(d) Electric field components (absolute value) for the fundamental TM mode at an operating wavelength of 1.55 μm

$$\frac{\left|\iint_{A_\infty} \mathbf{E}(x,y;z)\cdot\mathbf{E}^*_{\mathrm{ref}}(x,y)\,dxdy\right|}{\iint_{A_\infty}|\mathbf{E}_{\mathrm{ref}}(x,y)|^2 dxdy}. \tag{12}$$

Note that in Eq. (3) ref stands for reference and not reflected as in the equations of Section 2. We evaluate the aforementioned overlap integral at several z-points along the waveguide and the result is presented in Figure 4(a) for both the proposed and default ABCs. Clearly, the proposed ABC permits the correct excitation and absorption of the mode in question. On the other hand, when the default ABC is used, a standing wave pattern is formed.

Finally, let us note that the faint ripple in the transverse (E_x and E_y) components, and consequently in the overlap integral, is associated with the axial mesh density, and does not have anything to do with a standing wave. This can be readily confirmed by the period of the ripple ($\sim\lambda_g/20$). The piecewise-constant approximation in the axial component (E_z) is a demonstration of the well-known mixed-order principle.

3.2 CGS Waveguide

As a second example, we examine a very recently proposed type of plasmonic waveguide, namely the CGS waveguide [11, 12]. The waveguide cross-section is depicted in Figure 5(a). It consists of a gold cap (refractive index is taken from Ref. [13] and equals $0.55 - j11.5$) on top of a silicon ridge separated by a silica layer (gap). This three-region guiding ridge resides on a silica substrate. The CGS waveguide offers some distinct advantages compared with other plasmonic waveguides. Specifically, it provides deep subwavelength confinement, while at the same time featuring tolerable propagations losses, that is, resistive losses in the gold cap. Moreover, it permits a seamless transition to and from silicon waveguides [12]. This attribute is very important, as efficient merging of the two most prominent technologies for nanophotonics, namely plasmonics and silicon photonics, can allow for exploiting the unique advantages of each one.

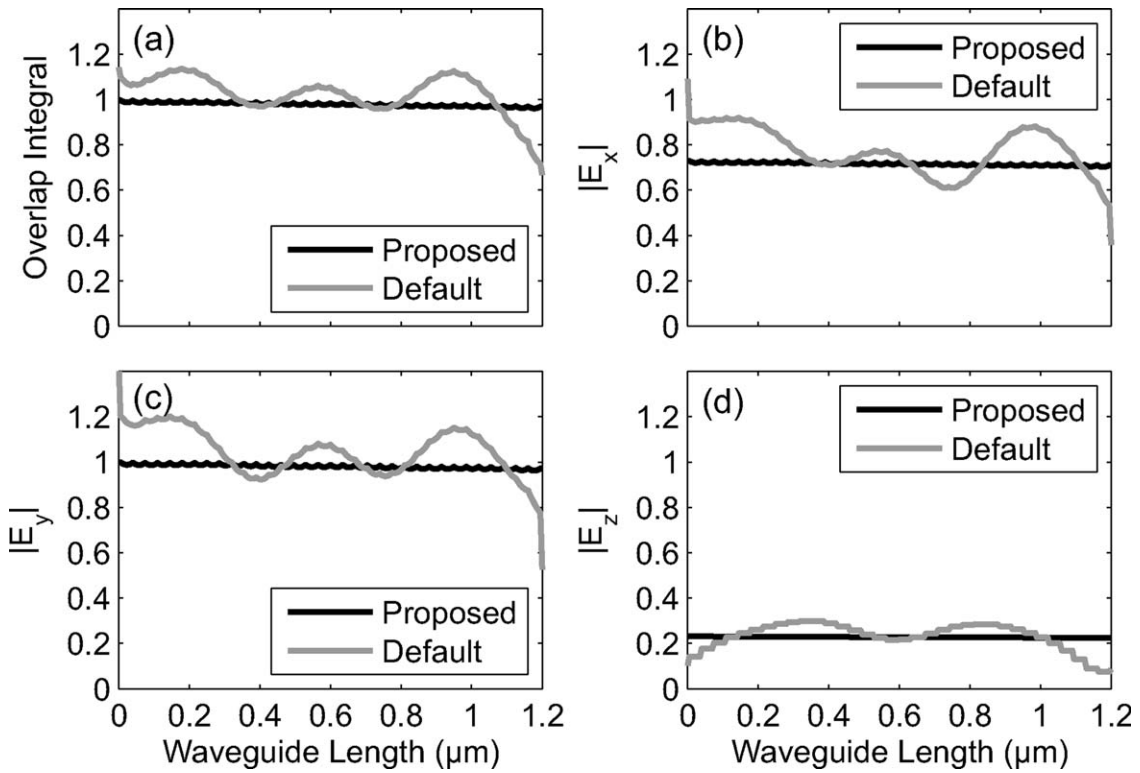

Figure 6 Comparison between proposed and default absorbing boundary conditions for a 1.2-μm-long CGS plasmonic waveguide operating on the fundamental TM mode at the 1.55 μm telecommunication wavelength. (a) Overlap integral along the waveguide, and (b)–(d) absolute value of electric field components along the waveguide. Each component is evaluated at the cross-sectional point associated with its peak value

In this example, the width of guiding ridge is equal to 200 nm. Moreover, the height of the silicon, silica and gold layers are 340, 50, and 50 nm, respectively. Therefore, the total height of the guiding ridge is $h = 440$ nm. The fundamental mode in this case is TM-like, meaning that it is the E_y component that is dominant. Figure 5(b)–(d) depicts the absolute value of the electric field components corresponding to the fundamental TM mode for an operating wavelength of 1.55 μm, as obtained by the solution of the 2D eigenvalue problem. The distribution of the dominant electric field component (E_y) reveals that most of the mode energy is guided inside the 200×50 nm^2 silica layer, verifying that the confinement is indeed subwavelength. Again, the hybrid nature of the mode in question is evident by noting the relative amplitude of the transverse electric-field components and the fact that both axial field components (electric and magnetic) are nonzero.

Turning to the 3D-guided-wave problem, plots (b)–(d) in Figure 6 depict the absolute value of the electric-field components along the waveguide, for both the proposed and default ABCs. The length of the waveguide segment considered is $L = 1.2$ μm, corresponding to ~ 1.61 λ_g for the mode in question ($\lambda_g = 0.747$ μm at the free-space wavelength of 1.55 μm). In addition, in Figure 6(a) the overlap integral along the waveguide is depicted. As with the previous example, the proposed ABC permits the correct excitation and absorption of the mode in question, and thus a purely guided wave is propagating in the structure. On the other hand, when the default ABCs are used, a standing wave pattern is formed, owing to reflections from the two ports. One might also notice that when the standard ABCs are used, both transverse electric field components are excited with higher amplitudes than dictated by the solution of the 2D eigenvalue problem. This is because at the cross-sectional points associated with their peak value, η_0/n_{eff} is smaller than both Z_w^{TM} and Z_w^{TE}. On the contrary, in the previous example of a silicon wire waveguide, E_x is excited with a lower amplitude, as $\eta_0/n_{\text{eff}} > Z_w^{\text{TE}}$ at the respective cross-sectional point. Finally, let us note that the slight negative slope evident in the field component and overlap integral plots is because of propagation (resistive) losses. Specifically, for the waveguide dimensions considered, the propagation length, that is, the distance at which the optical intensity has dropped by a factor of e^{-1}, is ~ 23 μm.

4. CONCLUSION

A boundary condition capable of efficiently exciting and absorbing hybrid waveguide modes has been developed for use in the context of the FEM. The proposed boundary condition is simple and can be readily implemented in existing finite element codes with minimal effort. It can be viewed as a generalization of the standard ABC which is correct only when the wave impedance of a given mode is scalar, spatially constant, and equal to η_0/n_{eff}. However, instead of wondering whether this assumption holds, and to what extent, it is much safer using the proposed ABC which is valid for any kind of mode, hybrid or not.

The performance of the proposed ABC has been tested in two examples: a silicon wire operating on the fundamental TE-like mode, and a CGS plasmonic waveguide operating on the fundamental TM-like mode. In both cases its performance was found to be exceptionally good.

ACKNOWLEDGMENT

This work was supported by the ''Heracleitus II'' research funding program, co-financed by the European Union and Greek national funds.

REFERENCES

1. J.-M. Jin, The finite element method in electromagnetics, Wiley, New York, 2002.
2. J. Liu, J.-M. Jin, E.K.N. Yung, and R.S. Chen, A fast, higher order three-dimensional finite-element analysis of microwave waveguide devices, Microwave Opt Technol Lett 32 (2002), 344–352.
3. A.S. Polycarpou, P.A. Tirkas, and C.A. Balanis, The finite element method for modeling circuits and interconnects for electronic packaging, IEEE Trans Microwave Theory Tech 45 (1997), 1868–1874.
4. M. Lu and P.J. Leonard, On the field patterns of the dominant mode in unilateral finline by the finite-element method, Microwave Opt Technol Lett 38 (2003), 193–195.
5. Y. Li and Z.J. Cendes, High-accuracy absorbing boundary condition, IEEE Trans Magn 31 (1995), 1524–1529.
6. J.-M. Jin and N. Lu, Application of adaptive absorbing boundary condition to finite-element solution of three-dimensional scattering, IEE Proc Microw Antennas Propag 143 (1996), 57–61.
7. T. Ozdemir and J.L. Volakis, Triangular prisms for edge-based vector finite element analysis of conformal antennas, IEEE Trans Antennas and Propag 45 (1997), 788–797.
8. R.D. Graglia, D.R. Wilton, A.F. Peterson, and I.-L. Gheorma, Higher order interpolatory vector bases on prism elements, IEEE Trans Antennas Propag 46 (1998), 442–450.
9. D.I. Karatzidis and T.V. Yioultsis, Efficient analysis of planar microwave circuits with mixed-order prism vector finite macroelements, Int J Numer Model 21 (2008), 475–492.
10. W. Bogaerts, S.K. Selvaraja, P. Dumon, J. Brouckaert, K. De Vos, D. Van Thourhout, and R. Baets, Silicon-on-insulator spectral filters fabricated with CMOS technology, IEEE J Sel Top Quantum Electron 16 (2010), 30–44.
11. D. Dai and S. He, A silicon-based hybrid plasmonic waveguide with a metal cap for a nano-scale light confinement, Opt Express 17 (2009), 16646–16653.
12. M. Wu, Z. Han, and V. Van, Conductor-gap-silicon plasmonic waveguides and passive components at subwavelength scale, Opt Express 18 (2010), 11728–11736.
13. E.D. Palik (Ed.), Handbook of optical constants of solids, Academic Press, New York, 1985.

CMOS QUADRATURE VCO USING THE INJECTION MOSFET COUPLING

Sheng-Lyang Jang, Yao-Ting Chiu, Chia-Wei Chang, and Ching-Wen Hsue

Department of Electronic Engineering, National Taiwan University of Science and Technology, 43, Keelung Road, Section 4, Taipei, Taiwan 106, Republic of China; Corresponding author: m9502216@mail.ntust.edu.tw

Received 15 February 2011

ABSTRACT: *This article presents a new quadrature voltage-controlled oscillator (QVCO). The LC-tank QVCO consists of two first-harmonic injection-locked oscillators (ILOs). The outputs of one ILO are injected to the gates of the MOS transistors on the other ILO and vice versa so as to force the two local oscillator (LOs) operate in quadrature. The injection metal-oxide-semiconductor field-effect transistors (MOSFETs) are also used as frequency tuning varactors. The QVCO has been implemented with the Taiwan Semiconductor Manufacture Company (TSMC) 0.18 μm complementary metal-oxide-semiconductor (CMOS) technology and the die area is 0.646 mm × 0.841 mm. At the supply voltage of 1.3 V, the total power consumption is 9.58 mW. The free-running frequency is tunable from 5.44 to 5.95 GHz as the tuning voltage is varied from 0.2 to 2.0 V. The measured phase noise at 1 MHz*